

**(1) Cover page**

**Final Technical Report**

Award Number: G19AP00019

Title: Initial Development of Alaska Community Seismic Velocity Models

Authors and Affiliations: Clifford Thurber  
Department of Geoscience  
University of Wisconsin-Madison  
1215 W. Dayton St.  
Madison, WI 53706  
Phone: (608) 262-6027, FAX: (608) 262-0693  
cthurber@wisc.edu

Term Covered by the Award: January 1, 2019 - December 31, 2019

## Initial Development of Alaska Community Seismic Velocity Models

### (2) Abstract

We have continued the development of community seismic velocity models (CVMs) for  $V_p$ ,  $V_s$ , and  $V_p/V_s$  for the state of Alaska. As in other regions, for example Southern California and New Zealand, such community models are instrumental for obtaining accurate earthquake locations and focal mechanisms and for seismic wave propagation simulations. Our effort is timely in terms of data availability, in particular from the IRIS Transportable Array deployment in Alaska, as well as data from other temporary arrays. The specific tasks that we proposed to carry out are as follows:

Task (a): Further augment the body-wave dataset. In addition to including new data for another year from the IRIS Transportable Array combined with Alaska network data, we incorporate body-wave data from the SALMON array (Tape et al., 2017) into our enlarged dataset. We also further increase the number of S-wave picks for earthquakes in the dataset. We employ a combination of manual and automatic picking.

Task (b): Enhanced tomographic methods: body waves. In addition to continuing our standard body-wave tomography inversions with two widely-used body-wave tomography codes, based on simul2000 (Thurber and Eberhart-Phillips, 1999) and tomoDD (Zhang and Thurber, 2003), we planned to incorporate selected Moho reflection data from active-source experiments such as TACT to constrain crustal thickness.

Task (c): Further joint body wave-surface wave inversions. We will add the new body-wave data to our joint inversion analysis. Such joint inversions take advantage of the relatively complementary resolution of structure afforded by the two data types. We will continue to assess the results from two different inversion codes that make different approximations (Fang et al., 2016; Eberhart-Phillips and Fry, 2017). Neither of these codes has received widespread use, so we believe it is important to further benchmark their results against each other. We can also use the differences between the results to provide estimates of model uncertainties.

Task (d): Further joint seismic-gravity inversions. For this task, we apply and evaluate a joint inversion of surface-wave and gravity data using a code based on tomoDD (Syracuse et al., 2017).

Task (e): Incorporation of information from receiver functions. Although at present we are not proposing formal joint inversions including receiver functions, we planned to experiment with including Moho converted-wave S-P times from receiver function analyses as if they were actual S-P times from sources at the Moho interface. The absolute positions of the piercing points for the direct P and converted S are obviously not known *a priori*, and initially for simplicity we will have to assume that the two points are co-located. The approximate position of the appropriate point can be determined by ray tracing from the receiver down to the Moho and arriving at the Moho with an appropriate incidence angle (Prothero and Steck, 1991).

Task (f): Release of Alaska CVM version 1.0. We plan release version 1.0 of the Alaska CVM, consisting of values of  $V_p$ ,  $V_s$ ,  $V_p/V_s$ , and their estimated uncertainties at a set of points in latitude, longitude, and depth. This initial release will be in a simple tabular form, with an accompanying report documenting the manner in which the information was derived. It will be distributed through the IRIS Earth Model Collaborations, posted on one or more web sites, and included as an electronic supplement in a publication.

The above tasks build directly on the work we carried out under USGS award G18AP00017. Those tasks were: augmentation of the Eberhart-Phillips et al. (2006) body-wave dataset, augmentation of the available surface-wave dataset, tomographic inversion of the augmented body-wave dataset, tomographic inversion of the augmented surface-wave dataset, joint body wave-surface wave inversions, velocity model refinement with gravity, and preliminary joint seismic-gravity inversion. The 2018 and 2019 tasks contribute directly to the development of community seismic velocity models for Alaska. In turn, the models will be of fundamental value for the determination of accurate earthquake locations and focal mechanisms and for improving ground motion simulations, all of which contribute to improved earthquake hazard estimation. Here we report in detail on our accomplishments related to the above tasks.

### (3) Main body of the report

#### *Significance of the Project*

The significant contribution of this project is the development of three-dimensional (3-D) community seismic velocity models for P- and S-wave seismic velocity ( $V_p$  and  $V_s$ ) and their ratio ( $V_p/V_s$ ) for Alaska. Such work is indicated as a priority task in the EHP Program Announcement, in the second sentence under PNA Element II (*italics added*):

PNA Element II. Earthquake information, monitoring, and notification.

- Develop region-specific relationships for inferring seismic wave velocities from seismic or rock type data. *Develop 3-D community seismic velocity models for Alaska that are validated against earthquake catalog data to support improving earthquake locations, simulating ground motions, determining source mechanisms, evaluating sedimentary basin ground motion amplification and the calculation of probabilistic hazard maps.*

As in other seismically active regions such as Southern California and New Zealand, 3-D community seismic velocity models are valuable for improving earthquake locations and source mechanisms and are essential for improving ground motion simulations (Eberhart-Phillips et al., 2010; Lee et al., 2014; Shaw et al., 2015). This award, G19AP00019, supported the continuation of our effort to develop community seismic velocity models for Alaska. The original region for our 2018 work is indicated in Figure 1, but we have now analyzed data and developed models nearly state-wide for our 2019 effort.

#### *Research accomplished under award G19AP00019*

Task (a): Further augment the body-wave dataset.

We combine data from recent (IRIS Transportable Array, SALMON experiment, onshore Alaska Amphibious Community Seismic Experiment (AACSE) stations) and past temporary deployments with data from permanent stations (Figure 2a) in assembling our body-wave dataset. Automatic picking of body waves on waveforms of ~5,000 earthquakes in Alaska (Figure 2b) using the REST algorithm (Lanza et al., 2019) results in a large dataset of P-wave and S-wave wave arrival times. These data are combined with previous active source data (Eberhart-Phillips et al., 2006) and AEC analyst picks for use in body-wave tomography. Details on the new data follow.

We selected ~700 earthquakes during the onshore deployment period (~2018/05-2018/09) of the AACSE network (code XO) and ~650 earthquakes during deployment of the temporary USGS network for monitoring of the aftershocks of the December 2018 Anchorage earthquake (code GM, ~2019/01-2019/05). The complete data from the offshore AACSE stations were not available from IRIS until late 2019, unfortunately. We also extended our study region towards the southwest from longitude  $-164^\circ$  to  $-169.7^\circ$  and from latitude  $54$  to  $52.6^\circ$ . This covers a greater extent of the Aleutian volcanic arc and is more consistent with the extent of our study area for surface-wave tomography, so that we can jointly invert the two datasets. We downloaded waveforms for ~450 earthquakes in this region during 2016/07-2019/03. We did auto-picking of body waves using REST and quality control of P and S arrival times using Wadati diagram plots, as previously. We discarded all S picks at distances  $> 250$  km for crustal earthquakes ( $< 45$  km depth) to avoid the difficulty of picking the weak  $S_n$  phase in the P coda. A map of the station distribution is shown in Figure 2a.

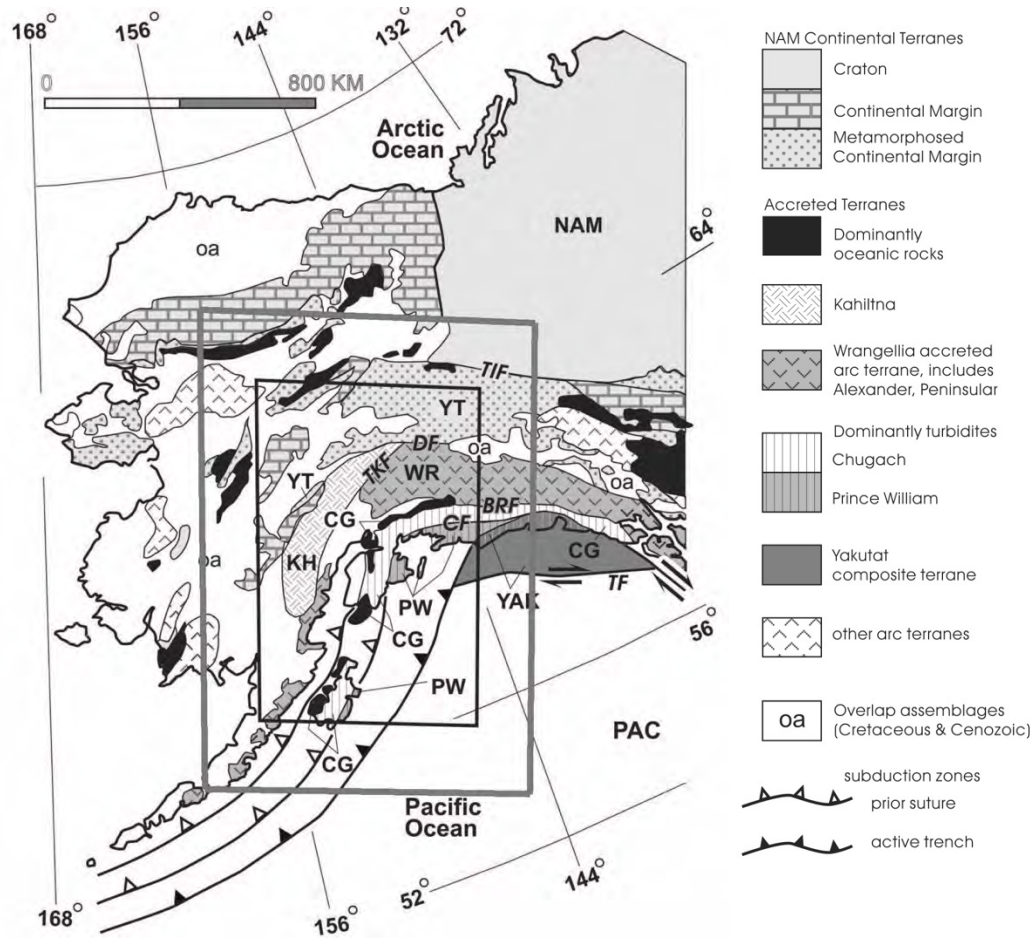


Figure 1. (a) Geologic map of our original study area for 2018 (larger gray rectangle) compared to the smaller region studied by Eberhart-Phillips et al. (2006) (smaller black rectangle).

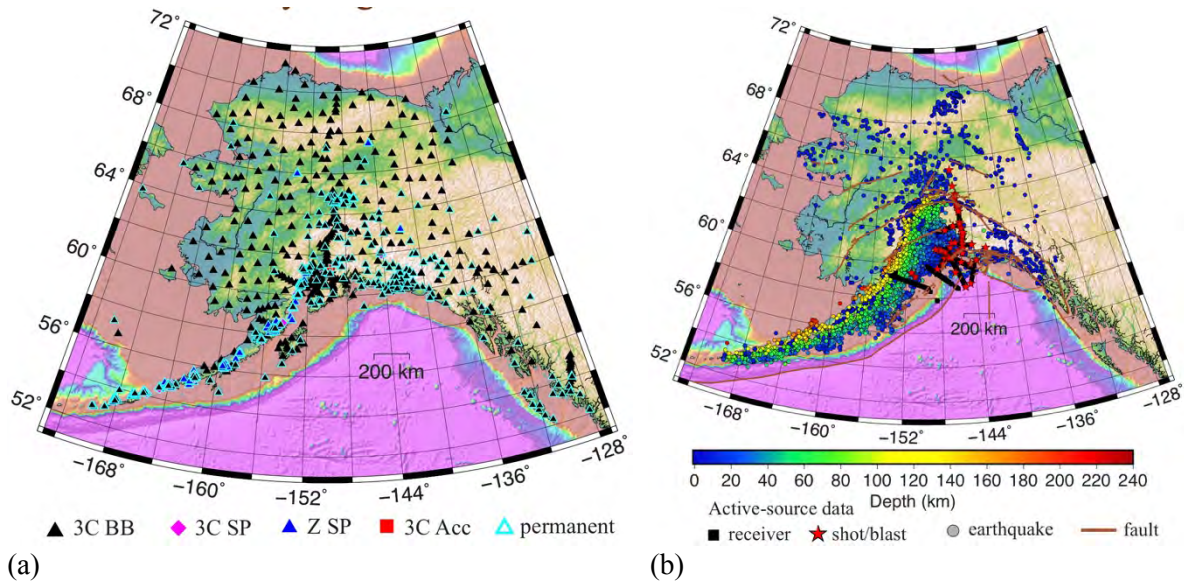


Figure 2. (a) Map of stations used for the assembly of our body-wave and surface-wave datasets. (b) Map of earthquakes (circles, color-coded by depth) and explosions (red stars) included in our body-wave dataset. Analyses have been carried out nearly state-wide in 2019.

The new picks were merged with body-wave data prepared in the previous year of the project. To keep the tomography computationally manageable, we selected an optimum number of earthquakes in each grid cell in the subduction zone region to have a more uniform spatial density of earthquakes for body-wave tomography. The final dataset containing ~5,500 earthquakes with at least 20 P and 3 S picks for each earthquake was combined with P-wave picks from the active source dataset (~122 shots and ~40 blasts) of Eberhart-Phillips et al. (2006) to assemble a final dataset of ~936,000 P-wave picks and ~299,000 S-wave picks. A map of the source distribution is shown in Figure 2b.

#### Task (b): Enhanced tomographic methods: body waves

We use a spherical earth version of tomoDD (Zhang et al., 2004) with ray tracing in spherical coordinates to invert for a state-wide body-wave velocity model of Alaska with grid spacing  $0.8^\circ$  in longitude and  $0.4^\circ$  in latitude (approximately 40 km). We tested 375 different combinations of damping and smoothing parameters to check the tradeoff between final misfit and model complexity. For the optimum combination of smoothing and damping parameters, our misfit decreased from ~1.5 s for an initial 1-D model to ~0.43 s for the final 3-D model, with gradual rejection of ~7% of the data as outliers (residual > ~2.3 s). Depth slices at 4 different depths are shown in Figure 3, with regions with low values of the node sampling measure, Derivative Weight Sum (Thurber and Eberhart-Phillips, 1999), masked out. We note that because the earthquakes are restricted to the crust in northern Alaska, we have little constraint on the deep S-wave velocity structure there from body waves. However, as we show later in this report, Vs structure in northern Alaska is adequately constrained by ambient noise derived surface waves. Our effort to include Moho (PmP) reflections in the tomographic inversion was not successful - see Task (e) for details.

#### Task (c): Joint body wave-surface wave inversions.

Two joint body wave-surface wave tomographic inversion efforts were carried out in parallel, using two different tomography algorithms that adopt different strategies for dealing with the surface-wave data. One algorithm is described in detail by Fang et al. (2015) for the surface-wave modeling approach and by Fang et al. (2016) for the joint inversion approach.

The other algorithm is described in detail in Eberhart-Phillips and Fry (2017). Briefly, in the volume surrounding each Rayleigh wave group velocity (U) observation, numerous points are distributed for relating the U observation to the gridded 3-D tomography model, analogous to points along a ray path. The volume is scaled with the period of the U data. The partial derivatives at the points are computed using the U sensitivity kernels as a function of depth for Vp and Vs, with Vs related to Vp and Vp/Vs perturbations, allowing for the joint inversion for Vp and Vp/Vs.

##### *1. Joint inversion with the Fang et al. (2016) algorithm*

We took a two-step approach for the modeling using the Fang et al. (2015, 2016) methods. First, we derived an improved state-wide model using just surface-wave data. Then we carried out the joint inversion using the Fang et al. (2016) algorithm. We describe the surface-wave only analysis first.

We processed ambient noise cross-correlations for data from the ~26 onshore stations of the AACSE array (2018.139-2018.299) and the temporary USGS stations for the aftershock monitoring of the Anchorage earthquake (2018.341-2019.133) and added that data to our surface-wave dataset. We carried out multi-component ambient noise cross-correlations. We used a standard methodology that preserves relative amplitudes among the three components of



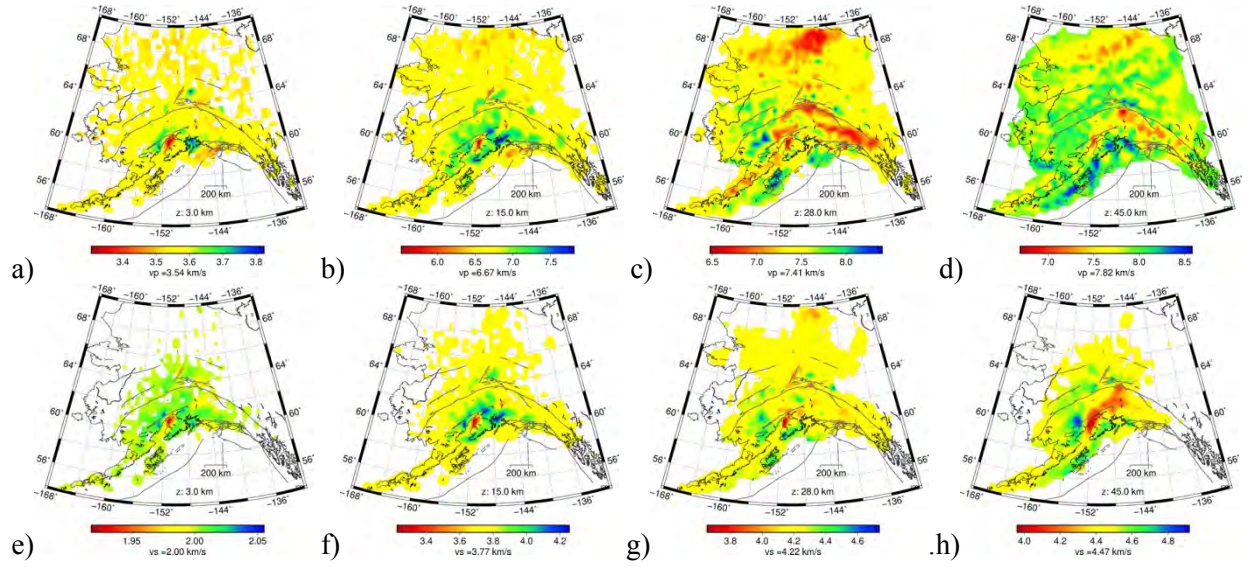


Figure 3. Depth slices through the body-wave only state-wide model at depths of 3, 15, 28, and 45 km for (a-d) Vp and (e-h) Vs. Velocity values in km/s, with the average velocity for that depth indicated.

motion (Lin et al., 2014) and allows us to rotate the cross-correlation tensors from the East-North-Vertical (E-N-Z) to the Transverse-Radial-Vertical (T-R-Z) reference frame. The four components in the radial-vertical plane (RR, RZ, ZR, and ZZ) were used to extract improved Rayleigh-wave dispersion measurements. The TT component was used to measure Love-wave dispersion. We applied automatic frequency-time analysis (AFTAN) methodology (Bensen et al., 2007, Lin et al., 2008) to the noise cross-correlations to extract the dispersion measurements. We started with group velocity dispersion measurements using a 1-D model as a reference.

We inverted Rayleigh-wave (periods  $\sim 5.2$  s to  $\sim 35$  s) and Love-wave (periods  $\sim 7.1$  s to  $\sim 35$  s) group velocity dispersion measurements to determine state-wide group velocity maps at each period with a grid spacing of  $0.4^\circ$  in latitude and  $0.8^\circ$  in longitude ( $\sim 40$  km), using the 2-D fast marching surface-wave tomography method (Rawlinson and Sambridge, 2004). For each latitude-longitude point in the maps, we jointly inverted the Rayleigh-wave and Love-wave group velocity dispersion for a vertical Vs profile using the surf96 algorithm (Herrmann, 2013). Group velocity at each period at each node was weighted by the Derivative Weight Sum at that node in the group velocity map at that particular period. Vp was scaled to Vs using Brocher (2005) relations in the inversion. Thereafter, we assembled a 3-D Vs model from the resulting set of 1-D models. Dispersion measurements in this period range are primarily sensitive to depths down to  $\sim 70$  km. In the next step, the 3-D velocity model was used as a reference model to measure Rayleigh-wave and Love-wave phase velocity dispersion using AFTAN. Phase velocities are more precisely measured and more consistent with eikonal equation based fast marching tomography method compared to group velocities. The Rayleigh-wave and Love-wave phase velocity measurements were inverted for 2-D phase velocity maps that were inverted for a revised 3-D model. This procedure of re-picking dispersion measurements, inverting for phase velocity maps, and inverting for a 3-D model was repeated one more time for full consistency.

The final state-wide phase velocity maps at representative periods are shown in Figure 4. For Rayleigh waves at each period, the number of dispersion measurements ranged from  $\sim 26,000$  to  $\sim 90,000$ , the final misfit varied from  $\sim 0.95$  s to  $\sim 1.3$  s, and the number of stations was  $\sim 790$ . For Love waves, the corresponding numbers are  $\sim 23,000$  to  $\sim 64,000$ ,  $\sim 0.95$  s to  $\sim 1.35$  s, and  $\sim 680$

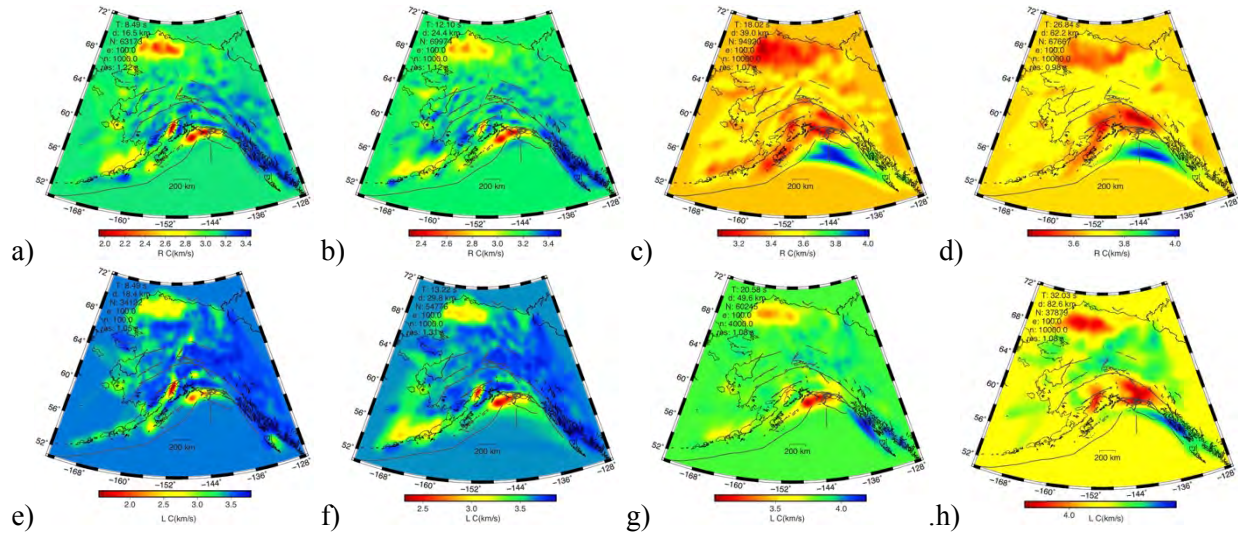


Figure 4. State-wide Rayleigh-wave phase velocity maps at representative periods of (a) 8.49 s, (b) 12.10 s, (c) 18.02 s, and (d) 26.84 s. State-wide Love-wave phase velocity maps at representative periods of (e) 8.49 s, (f) 13.22 s, (g) 20.58 s, and (h) 32.03 s. These results provide some of the data for the joint body wave-surface wave inversion.

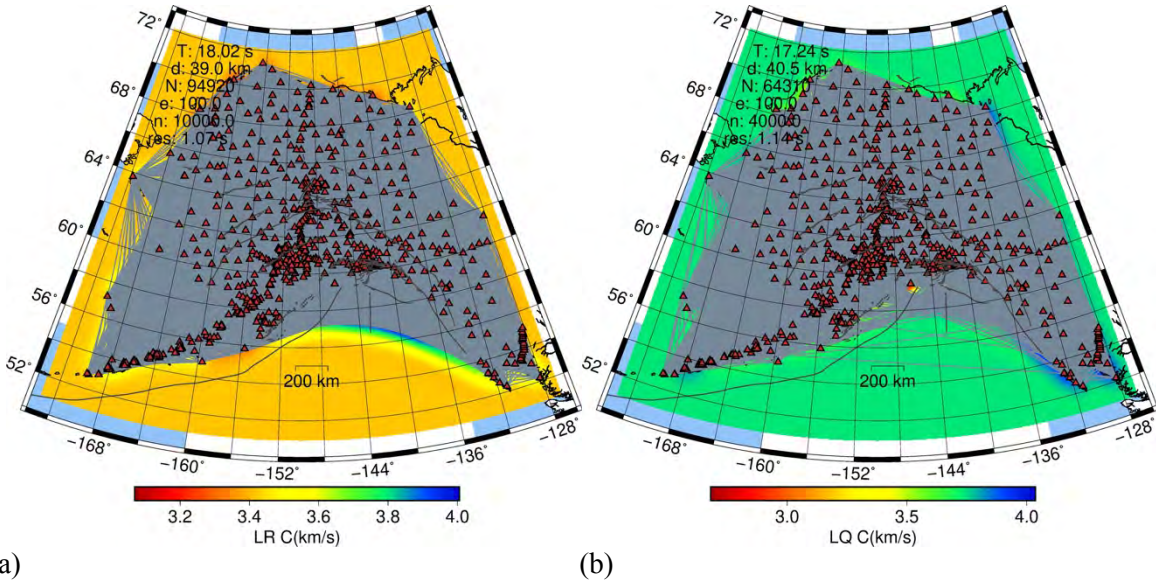


Figure 5. Example ray coverage maps for (a) Rayleigh waves at 18.02 s and (b) Love waves at 17.24 s.

stations. The phase velocity maps clearly delineate low-velocity basins even in offshore areas. The ray coverage for two of the better constrained periods are shown in Figure 5.

For the joint inversion of body-wave and surface-wave datasets for a state-wide velocity model of Alaska, we use the final earthquake locations and arrival times retained after removing outliers in the body-wave tomography. Rayleigh-wave and Love-wave phase velocity dispersion measurements at 17 and 15 distinct periods are selected in the surface-wave tomography period range. We use the same grid spacing of  $0.4^\circ$  in latitude and  $0.8^\circ$  in longitude ( $\sim 40$  km) as for the surface-wave phase velocity map inversions. We tested two initial models, the final model from surface-wave tomography and a weighted average of final models from body-wave and surface-wave tomography using Derivative Weight Sum (Thurber and Eberhart-Phillips, 1999) as



weights. We also tested the inversion without and with column normalization of the sensitivity matrix. An initial model derived from body-wave tomography was not tested in detail because of generally slower convergence of the surface-wave dataset compared to the body-wave dataset.

We revised the surface-wave section of the code used by Fang et al. (2016) to make it more efficient in order to accommodate the large surface-wave dataset. We also modified the code to adjust the relative weights between body-wave and surface-wave datasets at each iteration to enable faster convergence of both datasets. We have not tested the inversion for different damping and smoothing parameters because the joint inversion with the entire dataset is computationally demanding (the entire run of the code consumes  $\sim 110$  GB memory and takes  $\sim 1$ -3 days). The final misfit for the body-wave and surface-wave datasets were  $\sim 1.6$  s and  $\sim 0.4$  s, respectively, very close to the final misfit for the separate inversions of the two datasets. An additional  $\sim 4\%$  of the body-wave data was removed in the inversion as outliers (residual  $> 2.2$  s).

In the previous project year, 2018, we obtained surface-wave and arrival-time data for a smaller area and the Eberhart-Phillips et al. (2019) model (labeled DONNA18) was developed. Cross-sections through the final velocity model from the initial weighted-average model (without column normalization), designated AKA2020, are shown in Figure 6 compared to DONNA18,

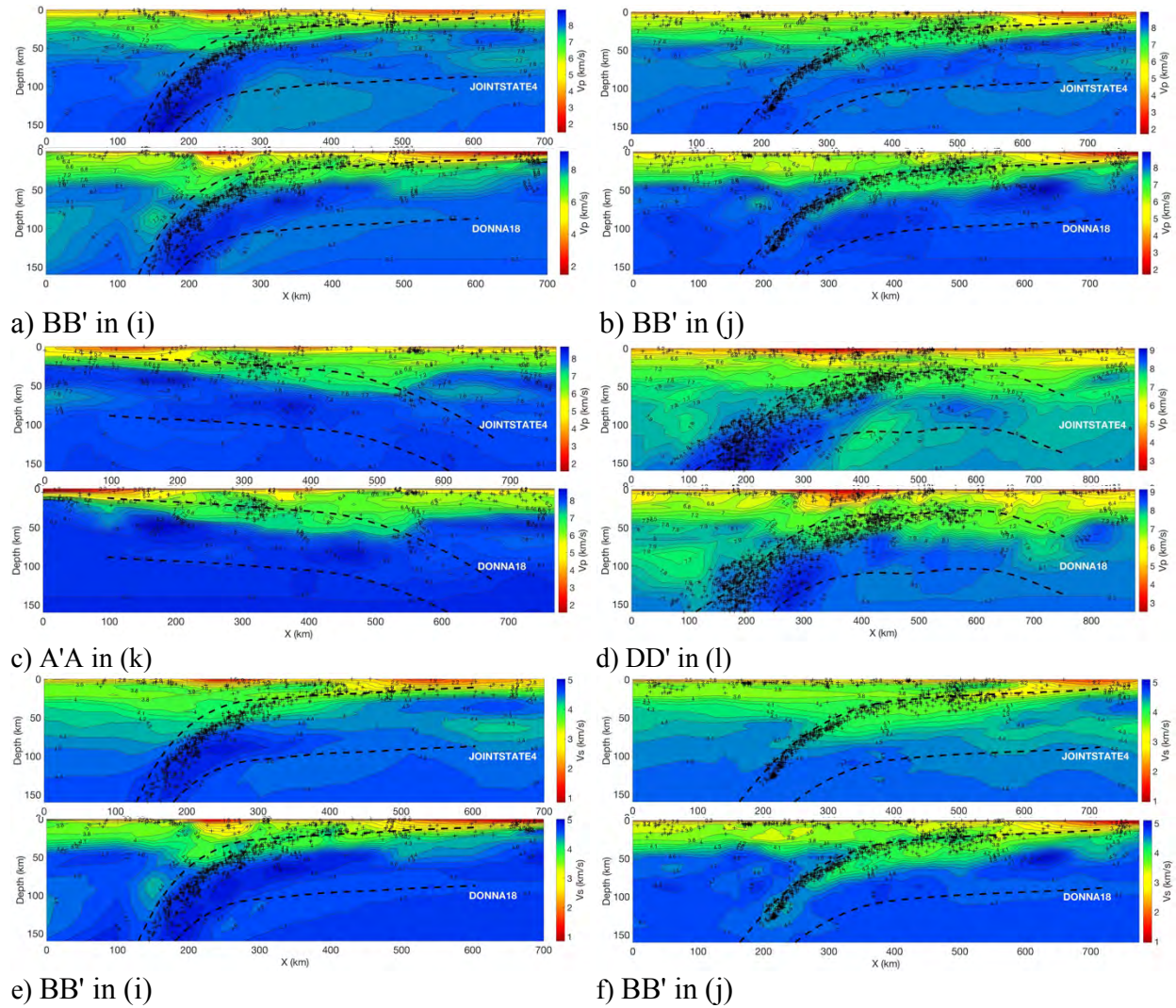


Figure 6 (continued).



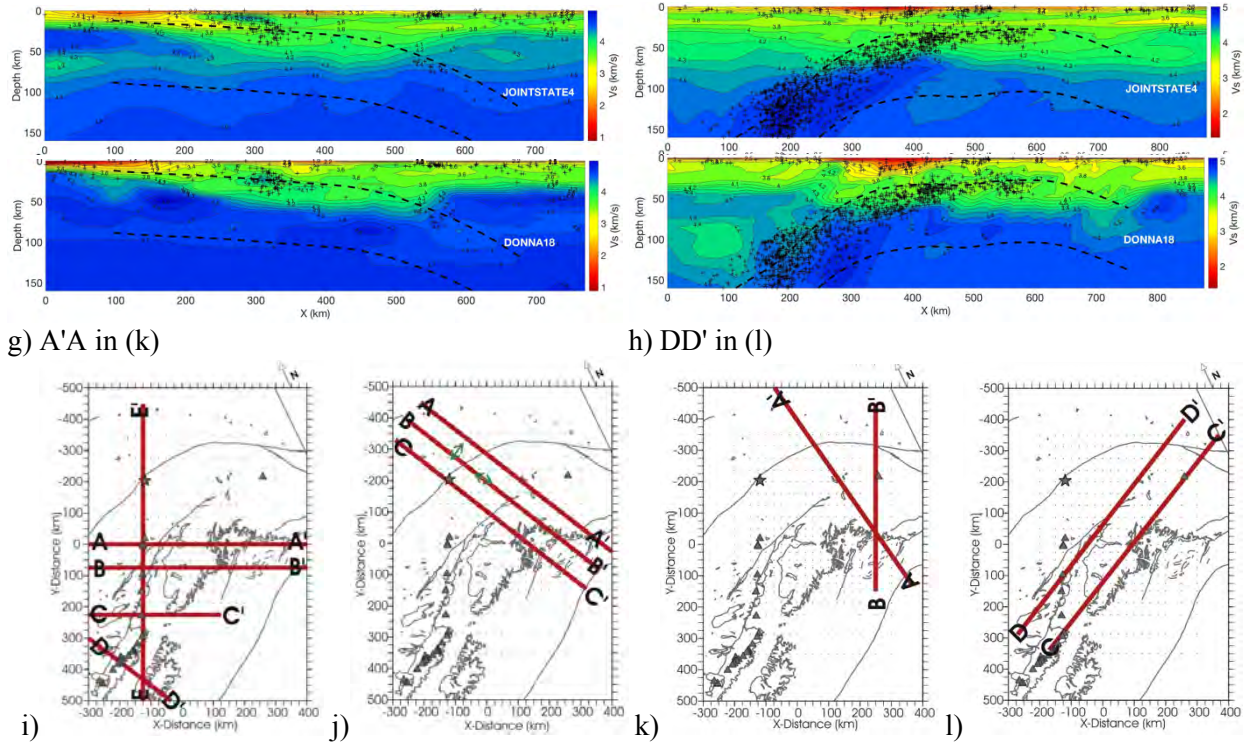


Figure 6. Cross-sections of (a-d) Vp and (e-h) Vs for model AKAN2020 (labeled JOINTSTATE4) compared to the model of Eberhart-Phillips et al. (2019) (labeled DONNA18), with Vs for the latter obtained by dividing Vp by Vp/Vs. (i-l) Maps showing cross-section locations, from Eberhart-Phillips et al. (2006). Cross-sections (a) and (e) are BB' in map (i), cross-sections (b) and (f) are BB' in map (j), cross-sections (c) and (g) are A'A' in map (k), and cross-sections (d) and (h) are DD' in map (l).

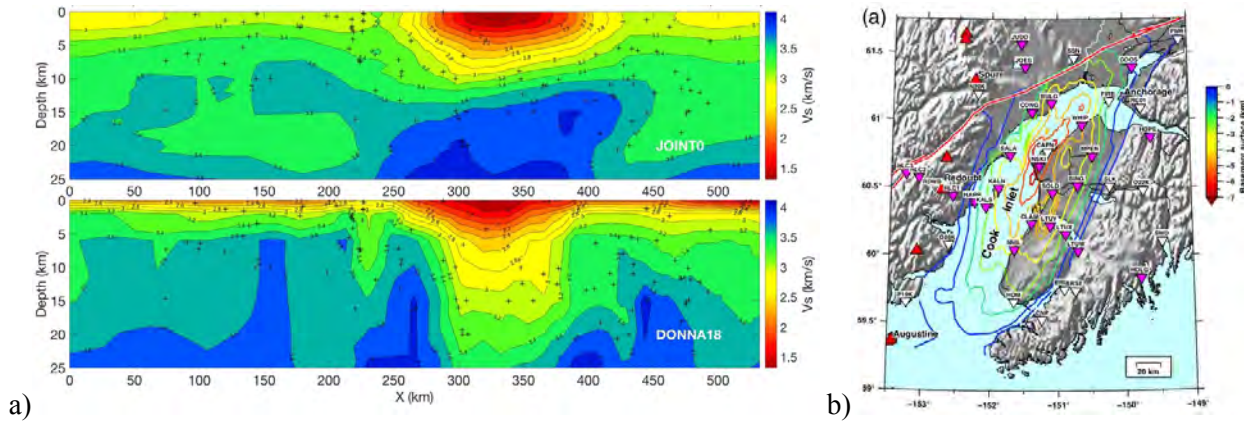


Figure 7. (a) Cross-sections spanning Cook Inlet through our model from joint inversion of Rayleigh- and Love-wave phase velocity measurements and body-wave arrival times using the method of Fang et al. (2016) compared to the model of Eberhart-Phillips et al. (2019). (b) Basement depth map of Cook Inlet from Schellenbaum et al. (2010).

along with maps showing the locations of the cross-sections, which match some of those presented by Eberhart-Phillips et al. (2006). Figure 7a shows cross-sections of the two models through the Cook Inlet basin compared to a basement depth map due to Schellenbaum et al. (2010) in Figure 7b. Model AKAN2020 from the revised Fang et al. (2016) code appears to produce a more accurate model for the depth of this basin. Otherwise, the two sets of models are

generally similar despite being obtained using completely different inversion algorithms,. A validation effort to assess which model result is superior would be valuable. We also used our model to relocate aftershocks of the 2018 Mw 7.1 Anchorage earthquake (Ruppert et al., 2020).

## *II. Joint inversion with the Eberhart-Phillips and Fry (2017) algorithm*

Simultaneous inversion for hypocenters and 3-D Vp and Vp/Vs structure has been done with a gradational approach, using arrival-time observations from the AK2006 study (Eberhart-Phillips et al., 2006) and recent data, and incorporating group velocity observations. Eberhart-Phillips (1990) developed the SIMULPS code to use P and S arrival-times to solve for Vp and Vs, through modifying the code of Thurber (1983). All S arrival-time ray-paths are calculated using the 3-D Vs structure in the Eberhart-Phillips (1990) code and all subsequent modified codes such as Eberhart-Phillips and Reyners (1997, 2012) and Eberhart-Phillips and Fry (2017). For typical earthquake arrival-time data, the Vs model is poorly constrained relative to the Vp model, less representative of crustal structure, and difficult to use for interpreting Vp/Vs (Eberhart-Phillips, 1989). Thus, as described by Eberhart-Phillips and Reyners (1997), it is preferable to solve for Vp and Vp/Vs when using local earthquake arrival-time data. This parameterization is retained for group velocity, with the Herrmann (2013) Vp kernels related to Vp model inversion parameters and Vs kernels related to partial derivatives of Vp and Vp/Vs model parameters (Eberhart-Phillips and Fry, 2017). Model Cartesian coordinates and distances are computed with Transverse Mercator conversion, and an earth-flattening transformation is used. The 0 km model depth is at sea level, travel-time ray-tracing includes station elevations, and elevation for group velocity observations is from the 30 km median topography (Figure 8a).

For this project, model AKEP2020 was developed, expanding on the data and area of the AKEP2006 model. This includes data from stations throughout Alaska and western Canada as shown in Figure 2a. Earthquakes and active source data from AKEP20006 are used. Selected earthquakes were included from the 2007-2008 MOOS array (Li et. al, 2013). Additional earthquakes from 2015/07 through 2019/03 were selected for spatial distribution and during periods of temporary arrays, primarily using data from the Alaska Earthquake Center (AEC). Additional REST autopicks were obtained. Many had large residuals and manual evaluation was not feasible in the project time frame, so down-weighting was applied after initial evaluation in the 3-D inversion code. For initial residuals > 2.7 s, data were eliminated. Picks had assigned quality codes of 0-4 (where 0 is best and 4 is unusable) and for initial residuals > 1.65 s, the pick quality code was increased by 3 to eliminate the most problematic observations. In contrast, for the earlier smaller central Alaska study (AKEP2006), arrival-time data were checked for each earthquake. The REST data provided about 39,000 P and 33,000 S observations. The expanded dataset included 4,953 earthquakes, and 162 active sources from TACT and EDGE studies (Figure 8b), totaling 413,776 P and 118,732 S observations. During the inversions, arrival-time data are linearly down-weighted for residuals of 0.5-1.2 s, and for distances of 75-600 km.

The 3-D velocity model is oriented parallel to the central Alaska subducted slab and extends 1600 km by 2000 km (Figure 8b), with coarsely spaced nodes near the periphery. A gradational approach is used for velocity inversions. This provides reasonable velocities throughout the region, and more detail where there is denser data coverage. The initial model used a coarse version of AKEP2006, with some extrapolation down the Alaska Peninsula, and very coarse models with recent data for distant areas. An inversion of the whole model area was done with ~50 km grid spacing. Then fine inversions were done with ~25 km grid spacing and auto-linking in low resolution areas (Eberhart-Phillips et. al, 2014) for the final body-wave model.

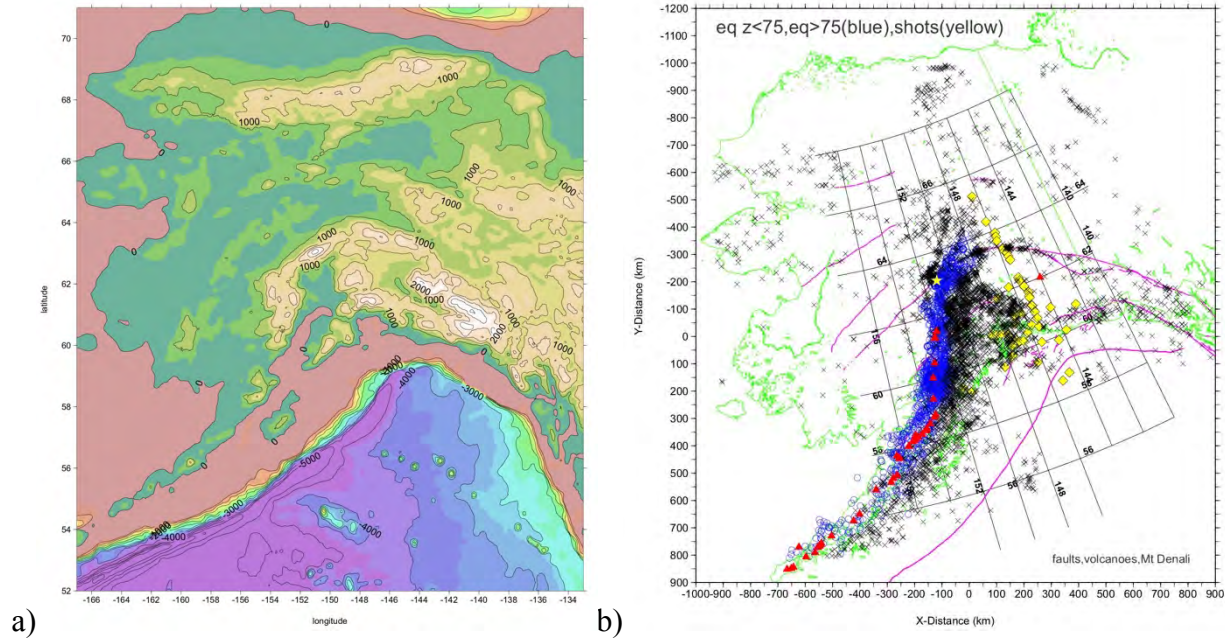


Figure 8. (a) Topography with a 30 km median filter applied used as elevations for group velocity observations. (b) Earthquake and shot distribution on a map showing the Cartesian coordinate system.

Then joint inversions of arrival-time and group velocity observations were completed to enhance the earthquake arrival-time model. Earthquake data has weak vertical resolution of the upper 6 km, although the velocity fits the arrival-time to the underlying earthquakes. Group velocity provides information at these shallow depths for  $V_p$  and  $V_s$ , for the 6-15 s periods of the selected observations, although it has inherent broad horizontal smoothing compared to the earthquake arrival-time data. The group velocity data incorporated 11,286 observations from group velocity maps, with quality assigned based on the Derivative Weight Sum of the underlying Rayleigh-wave path distribution (Figure 5a). A progressive series of joint inversions was done to promote improvement of the shallowest depths, with the deepest portions of the model fixed. The relative weight of the group velocity observations ( $wtU$ ) is varied. This series comprised (a) 1 iteration for depth  $z = -1$  km free and  $wtU=35$ ; (b) 2 iterations for  $z = -1, 2$  km free and  $wtU=22$ ; (c) 1 iteration for  $z = -1, 2, 6$  km free and  $wtU=10$ ; and (d) 2 iterations for  $z = -1$  through 33 km free and  $wtU=5.5$ . The final model achieves good improvement in fitting the expanded data set. Compared to the initial model, the final model AKEP2020 provides 36.4 % decrease in P data variance, 24.6% decrease in S-P data variance, and 96.7% decrease in group velocity data variance. The results are shown in map views for depths of 2-140 km for  $V_p$  in Figure 9 and for  $V_p/V_s$  in Figure 10. Cross-sections across the central Denali fault and across the Pacific-Yakutat slab boundary are shown in Figure 11, with comparison to AKEP2006. The cross-sections illustrate that  $V_p$ ,  $V_p/V_s$ , and  $V_s$  are all reasonable.

More work could be done to improve the quality of the arrival-time data, to assess the influence of specific group velocity observations on the results, and to test factors such as reducing the smoothing applied to group velocity maps during earlier processing of the dispersion data that provided group velocity. Varied approaches to the progressive inversions and the relative weight could be evaluated. Further evaluations are beyond the scope of this project. Such procedures would alter some specific model values and shapes of features, but overall the results would be similar.



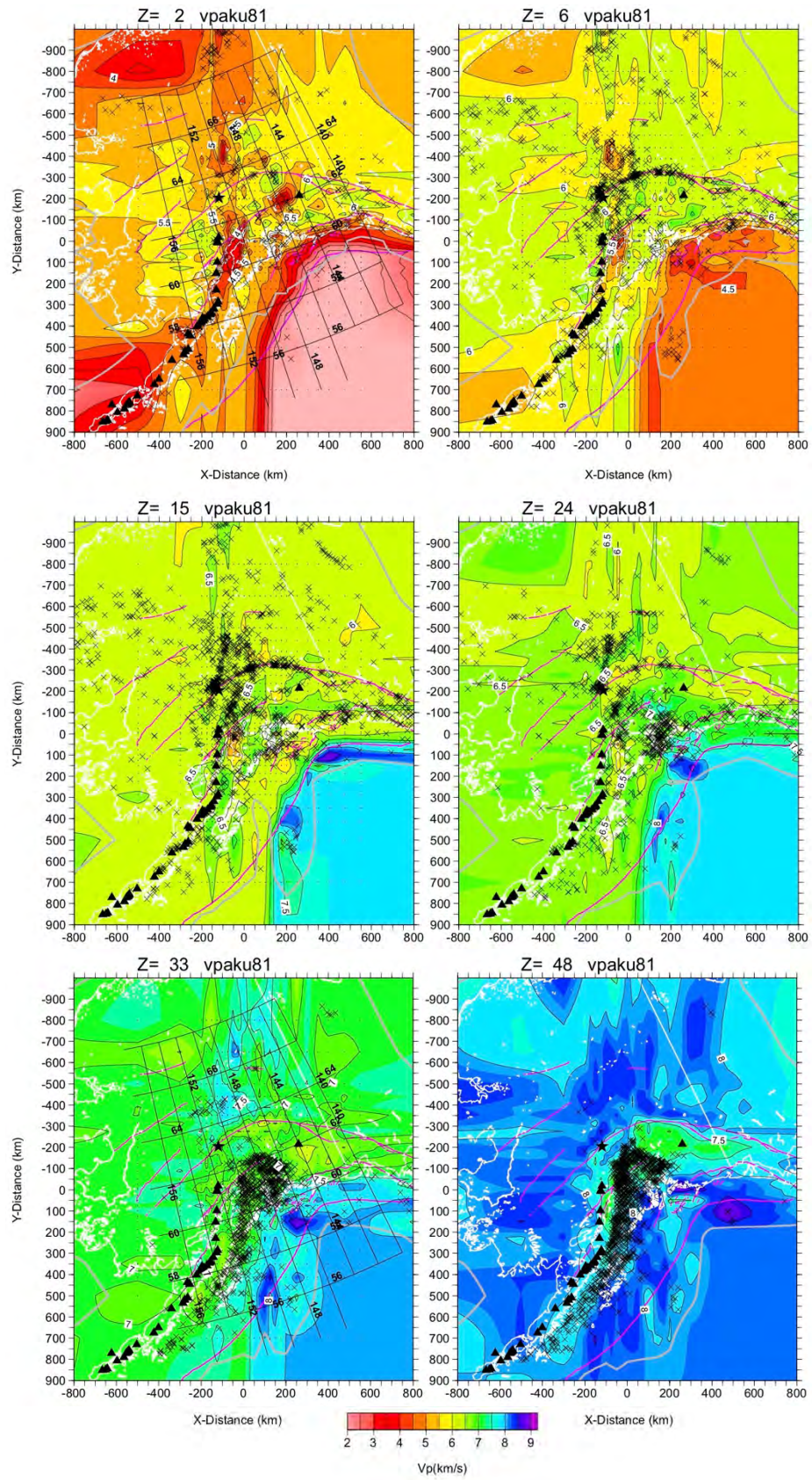


Figure 9 (continued)



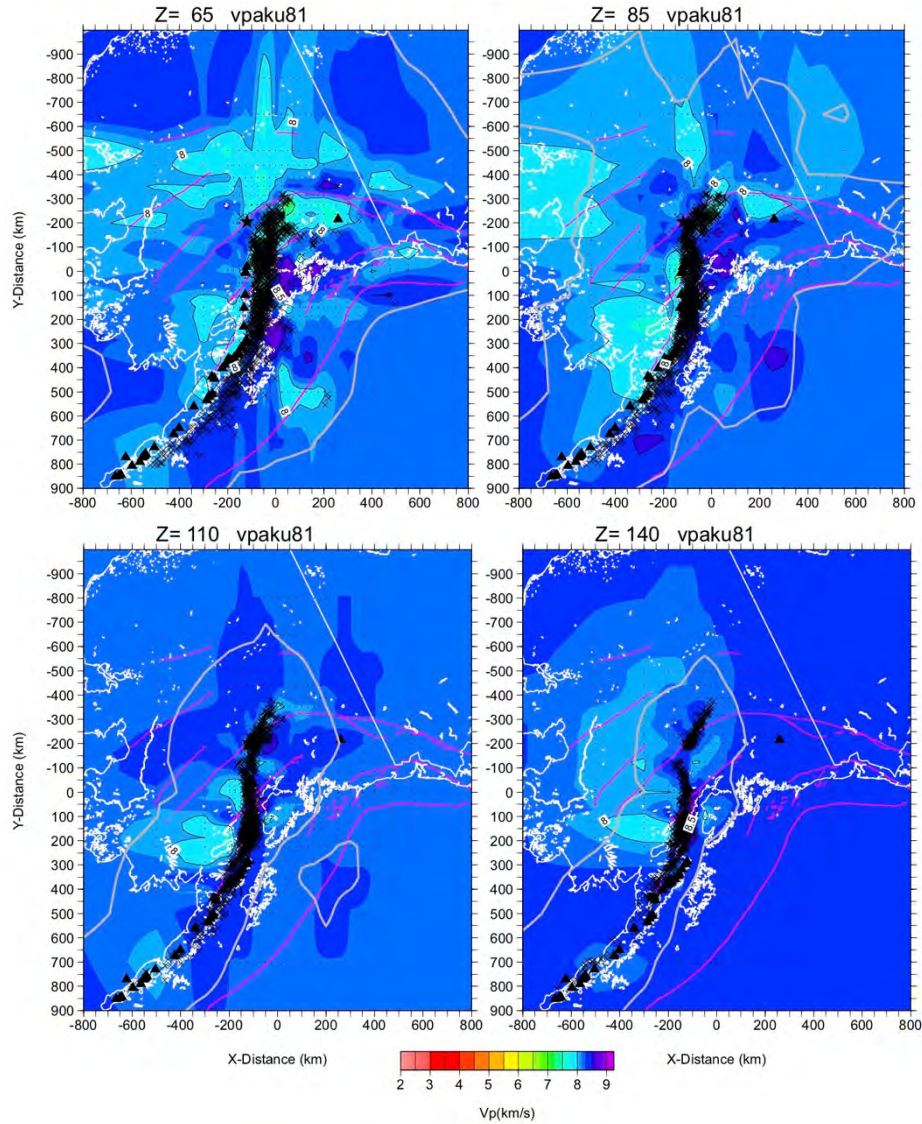


Figure 9. Vp maps, with gray line indicating the limit of adequate data for the 3-D grid model.

Compared to the AKEP2006 model, the new dataset allows for a much larger region of Alaska to be imaged successfully with both inversion algorithms. The model developed with the Eberhart-Phillips and Fry (2017) algorithm extends over an area of over 3 million square km compared to 750,000 square km for AKEP2006, although neither adequately covers the offshore area. The model developed with the Fang et al. (2016) algorithm images nearly the entire state, including some offshore areas but not including the western Aleutians. Incorporation of ocean bottom seismometer data from the AACSE (Abers et al., 2019) would allow imaging of structure out to the trench from approximately the Shumagin Islands to Kodiak Island.

#### Task (d): Joint seismic-gravity inversions.

We performed a joint inversion of seismic surface-wave data and gravity data to take advantage of different depth sensitivities of these two kinds of data in an effort to determine a more comprehensive and higher-resolution velocity model for basins. Specifically, we used period-dependent Rayleigh-wave group velocity map data and Bouguer gravity anomalies. The

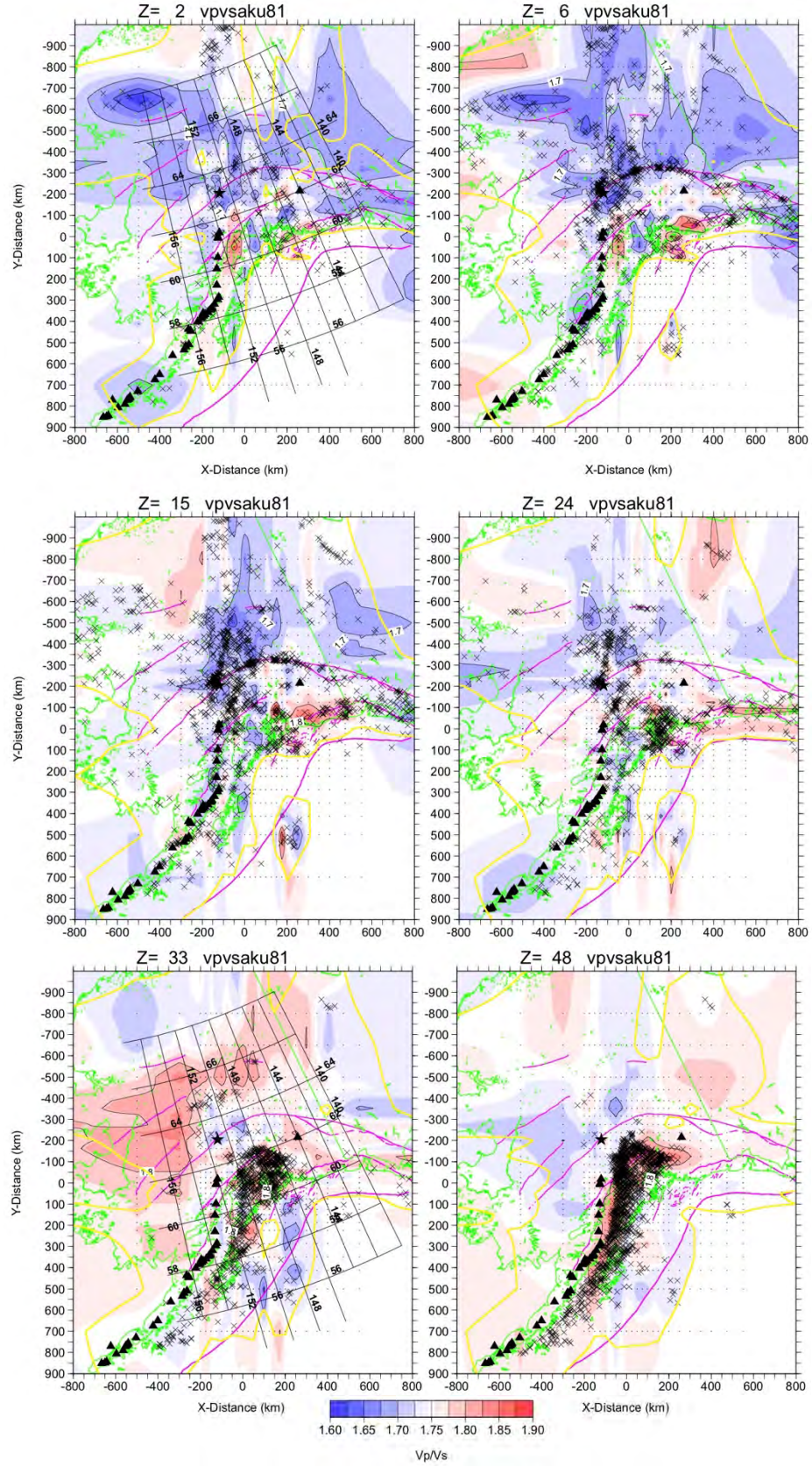


Figure 10 (continued)



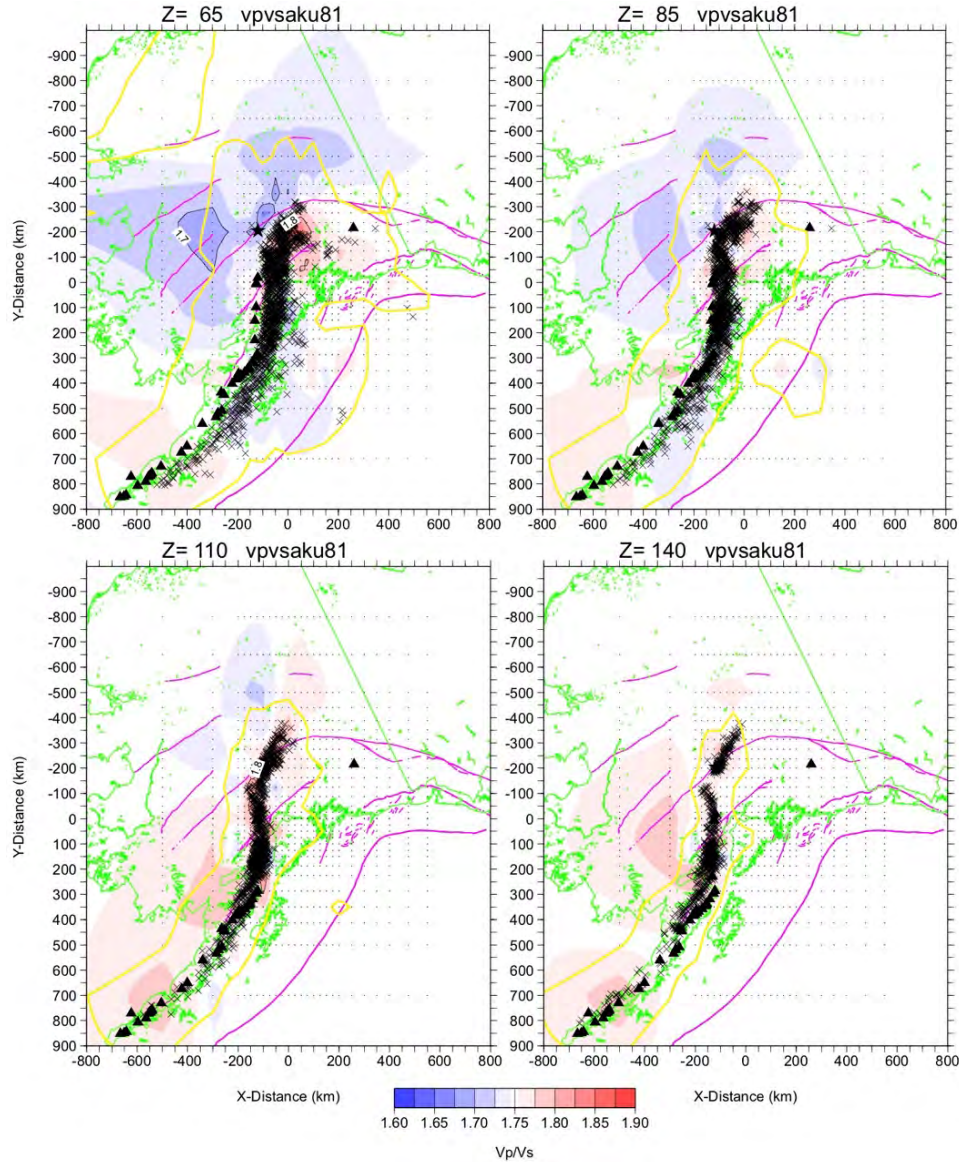


Figure 10. Vp/Vs maps, with gray line indicating the limit of adequate data for the 3-D grid model. Model nodes are shown as small gray plus symbols (+).

joint inversion yields basin shapes that differ from that derived from surface-wave data combined with either body-wave data or receiver function constraints. The study area is shown in Figure 12, indicating the locations of model cross-sections shown in later figures.

### Data

The Rayleigh wave group velocity maps were determined from the inversion of Rayleigh wave group velocity dispersion measurements. The Bouguer gravity anomalies were obtained from Bureau Gravimétrique International ([bgi.omp.obs-mip.fr](http://bgi.omp.obs-mip.fr)) and were extracted from the geographic-coordinate version of global model EMG2008 (Pavlis et al., 2012). We selected Bouguer anomaly data because the effect of topographic variation has been corrected so that it can be used by the joint inversion code, which does not take topography into account.

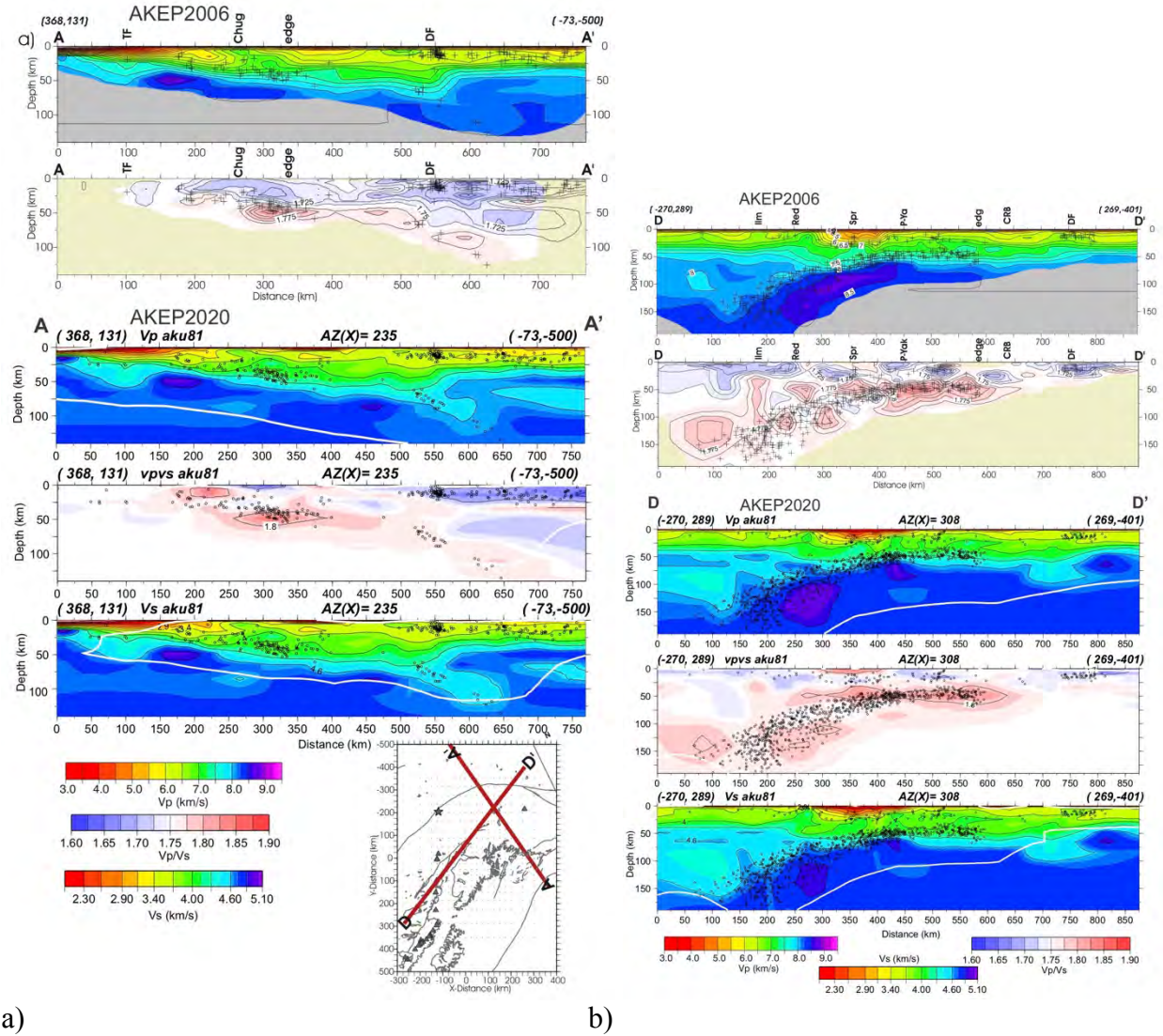


Figure 11. Upper two panels show AKEP2006, lower three panels show AKEP2020. (a) Vp and Vp/Vs cross sections with hypocenters (plus symbols) within 50 km of each section. Image is masked or has line where there is low resolution. (a) Normal to central Denali fault. (b) Across the Yakutat slab. TF, transition fault system; Chug, Chugach Mountains; DF, Denali fault; edge, apparent edge of Yakutat slab. Spr, Spurr; Red, Redoubt; Aug, Augustine; Ilm, Iliamna; CRB, Copper River basin; P-Yak, Pacific-Yakutat boundary.

### Method

We used the joint inversion algorithm JointTomoDD, which was developed based on the double-difference body-wave velocity tomography method tomoDD (Zhang and Thurber, 2003) by Syracuse et al. (2017). JointTomoDD can determine earthquake locations, 3-D Vp and Vs models, and a density model simultaneously by jointly inverting body-wave data, surface-wave data, and gravity data. Here, only surface-wave and gravity data are used for determining the Vs model. The joint inversion of surface-wave and gravity data follows the method of Maceira and Ammon (2009); the methodology is described briefly below.



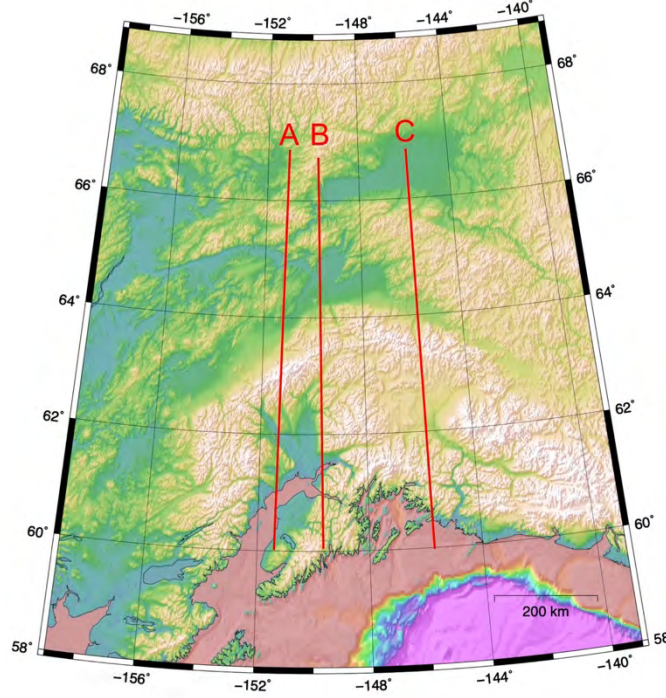


Figure 12. Map of the study area showing the locations of cross-sections shown in Figures 15-17.

The linearized, iterative inversion in JointTomoDD follows the form

$$Gm = d$$

where  $G$  is a matrix of partial derivatives,  $m$  is a matrix of model perturbations, and  $d$  is a vector of data. In the joint inversion of surface-wave and gravity data, this equation can be expressed as follows,

$$\begin{bmatrix} \mu G_{Vs}^{SW} \\ \eta G_{Vs}^B \end{bmatrix} [\Delta m] = \begin{bmatrix} \mu d^{SW} \\ \eta d^B \end{bmatrix}$$

where  $G_{Vs}^{SW}$  is a matrix of partial derivatives of surface-wave data with respect to  $V_s$  perturbations,  $G_{Vs}^B$  is a matrix of partial derivatives of Bouguer gravity data with respect to  $V_s$  perturbations,  $m$  is the  $V_s$  model,  $\Delta m$  is the  $V_s$  perturbations,  $d^{SW}$  is surface-wave data,  $d^B$  is the gravity data,  $\mu$  is the weight of surface-wave data, and  $\eta$  is the weight of gravity data. Note that the gravity-based partial derivatives are derived using an empirical relation between density and seismic velocity (Syracuse et al., 2017). Smoothing and damping constraints are used to regularize the above system of equations. The final system is solved with the LSQR solver (Paige and Saunders, 1982).

### *Inversion details*

Following the suggestion by previous studies using joint inversions involving gravity data (Maceira and Ammon, 2009; Syracuse et al., 2017), the gravity data are spatially filtered prior to the inversion by removing the mean gravity value of nodes within  $2^\circ$  of each node. This procedure can remove long-wavelength features from the gravity data that can be caused by deep density anomalies or by non-isostatically compensated structure (Syracuse et al., 2017) but still keeps sharp gravity gradients that can be caused by strong horizontal contrasts in density



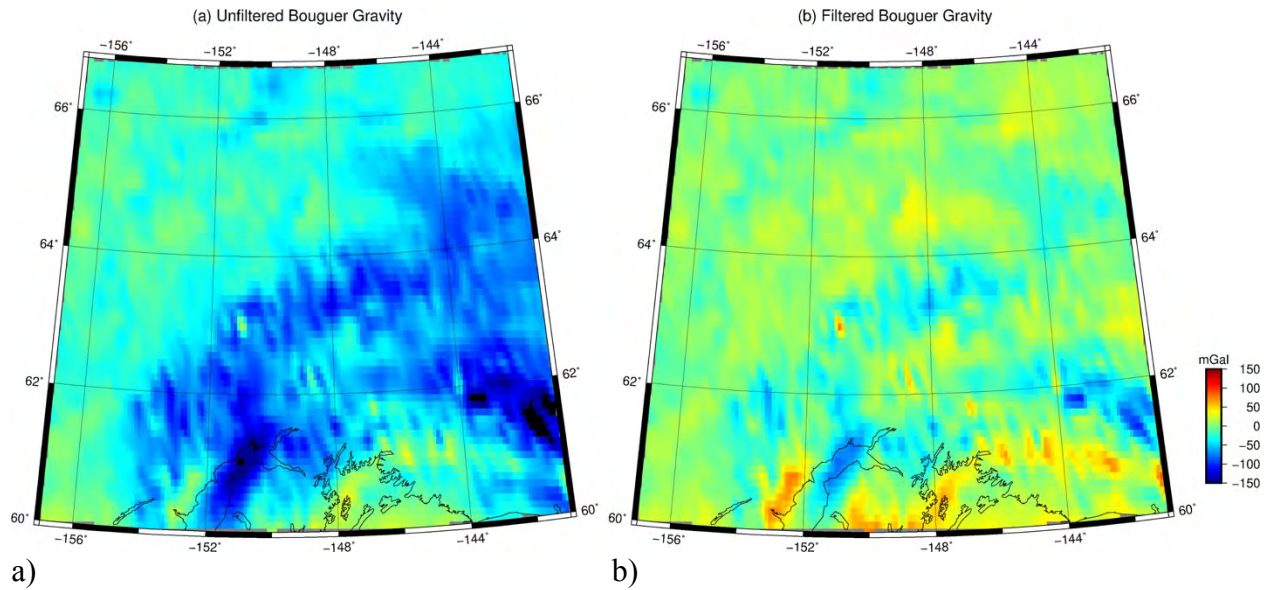


Figure 13. Maps of (a) unfiltered and (b) filtered Bouguer gravity anomalies in the study area (in mgals).

structure in the crust. Figure 13 shows the Bouguer gravity anomalies before and after filtering.

We started the inversion with Vs models from two previous studies. One is from the joint inversion of body-wave and surface-wave data by Eberhart-Phillips et al. (2019). Note that the surface-wave data used by Eberhart-Phillips et al. (2019) is the same as are used here. The other is from the joint inversion of surface-wave and receiver function data by Berg et al. (2020). During the inversion, we used the weights of surface-wave and gravity data similar to Syracuse et al. (2017). Four iterations were performed.

### Results

Figure 14 shows the comparison of the predicted Bouguer anomalies using different Vs models. It can be seen that the gravity data predicted with the Vs models of Eberhart-Phillips et al. (2019) and Berg et al. (2020) are apparently inconsistent with the observed, filtered gravity data, indicating these models inverted with seismic data alone cannot explain the gravity observations. After including the gravity data into the joint inversion, the improvement in fitting the gravity data can be seen, indicating that the gravity data play an important role in the joint inversion and that the joint inversion helps to determine a model that can explain both the surface-wave and gravity data reasonably well.

Figures 15-17 show the comparison of velocity models from Eberhart-Phillips et al. (2019), Berg et al. (2020), and this study for north-south cross-sections crossing the Cook Inlet Basin (CIB), Nenana Basin (NB), and Copper River Basin (CRB), respectively. We find that the results using different starting models are very similar, indicating our joint inversion is not sensitive to the initial model. Overall, our new model is generally similar to our joint body-wave and surface-wave inversion models, but with significant differences beneath some large basins.

Beneath the CIB, the model of Eberhart-Phillips et al. (2019) shows a low-velocity anomaly extending to a depth of ~20 km. This basin is also present in our model but is wider and its base is much shallower (<10 km depth). In comparison, our model is more similar to the model of Berg et al. (2020), but still has apparent differences regarding the width and thickness of the low-velocity basin. Beneath the NB, both of the models of Eberhart-Phillips et al. (2019) and Berg et al. (2020) show a low-velocity anomaly extending to a depth of ~15 km. This low-velocity body

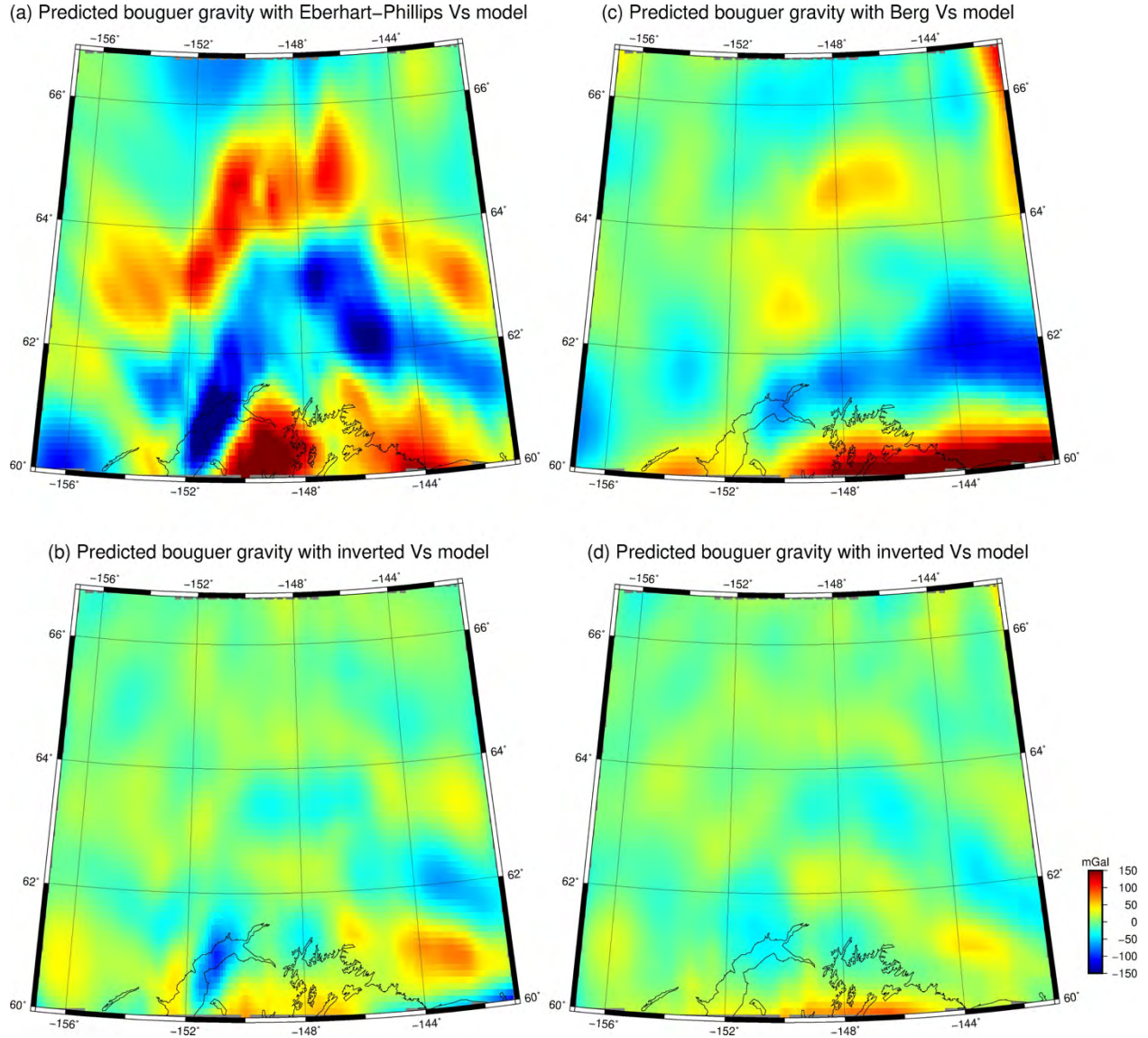


Figure 14. Comparison of the predicted Bouguer anomalies using different Vs models. (a) Predicted gravity from the Vs model of Eberhart-Phillips et al. (2019). (b) Predicted gravity from the Vs model obtained from the joint inversion starting from the Eberhart-Phillips et al. (2019) model. (c) Predicted gravity from the Vs model of Berg et al. (2020). (d) Predicted gravity from the Vs model obtained from the joint inversion starting from the Berg et al. (2020) model.

is also shown in our model but is again much shallower ( $< 10$  km depth). Beneath the CRB, the model of Eberhart-Phillips et al. (2019) shows a low-velocity anomaly extending to a depth of  $\sim 20$  km. This low-velocity basin in our model is again much shallower ( $< 10$  km depth), which is similar to the model of Berg et al. (2020). In addition, our model also shows that the low-velocity anomaly beneath the CRB appears to be connected to a deeper low-velocity anomaly beneath the coast.



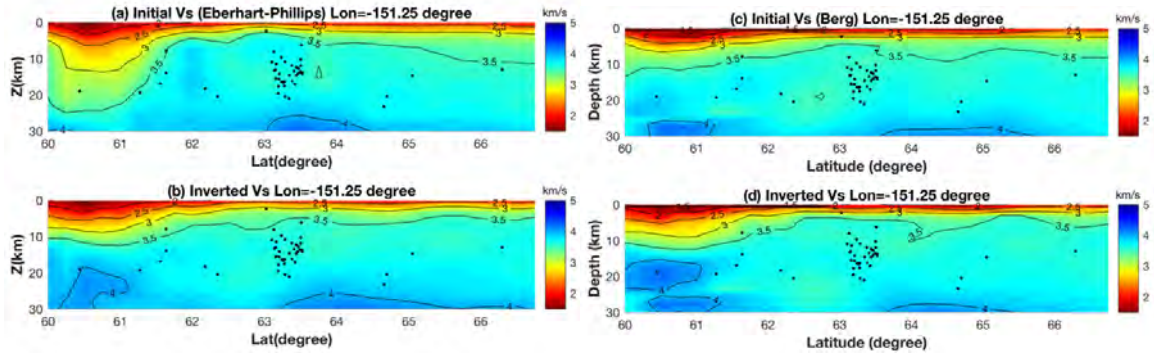


Figure 15. Cross-sections of the initial and inverted Vs models at longitude  $-151.25^\circ$ . (upper left) Vs model of Eberhart-Phillips et al. (2019). (lower left) Inverted Vs model starting from the Eberhart-Phillips et al. (2019) model. (c) Vs model from Berg et al. (2020). (d) Inverted Vs model starting from the Berg et al. (2020) model. Dots represent earthquakes within  $0.125^\circ$  of the cross-section, which is labeled A in Figure 12 and crosses the Cook Inlet Basin at a latitude of about  $60.5^\circ$ .

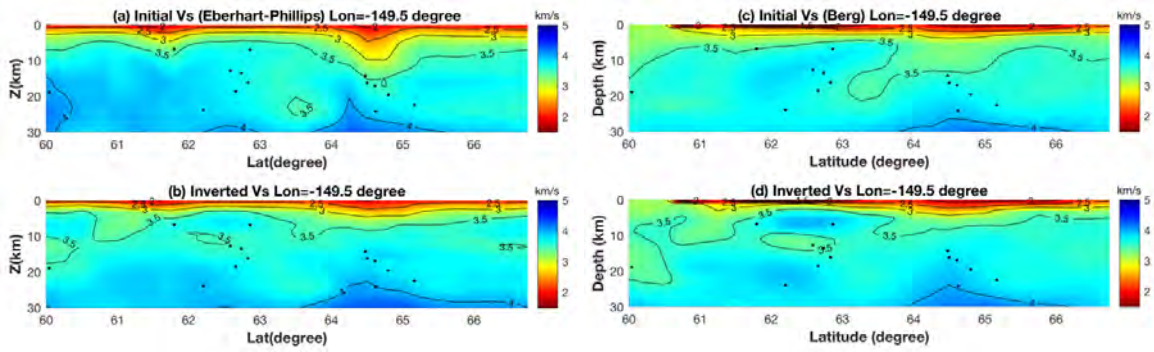


Figure 16. Cross-sections of the initial and inverted Vs models at longitude  $-149.5^\circ$ . (upper left) Vs model of Eberhart-Phillips et al. (2019). (lower left) Inverted Vs model starting from the Eberhart-Phillips et al. (2019) model. (c) Vs model from Berg et al. (2019). (d) Inverted Vs model starting from the Berg et al. (2019) model. Dots represent earthquakes within  $0.125^\circ$  of the cross-section, which is labeled B in Figure 12 and crosses the Nenana Basin at a latitude of about  $64.5^\circ$ .

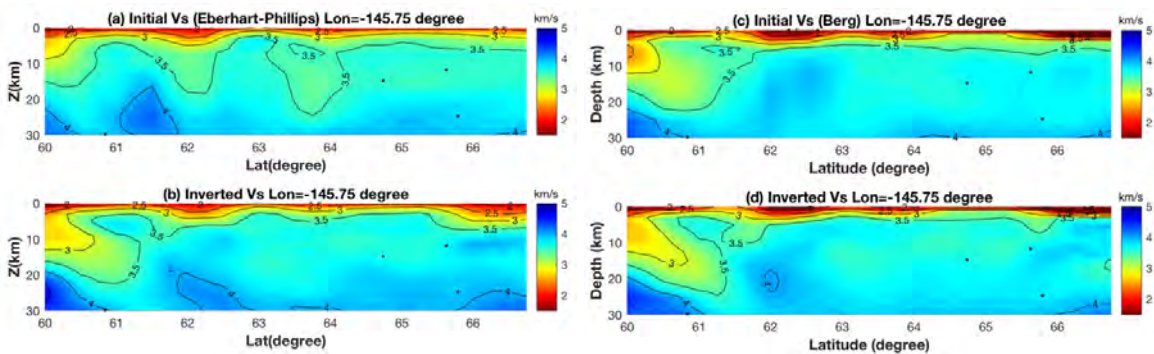


Figure 17. Cross-sections of the initial and inverted Vs models at longitude  $-145.75^\circ$ . (upper left) Vs model of Eberhart-Phillips et al. (2019). (lower left) Inverted Vs model starting from the Eberhart-Phillips et al. (2019) model. (c) Vs model from Berg et al. (2020). (d) Inverted Vs model starting from the Berg et al. (2020) model. Dots represent earthquakes within  $0.125^\circ$  of the cross-section, which is labeled C in Figure 12 and crosses the Copper River Basin at a latitude of about  $62^\circ$ .



Task (e): Incorporation of information from receiver functions.

Accomplishment of this task was contingent on first succeeding with the incorporation of PmP (Moho reflection) travel times from active-source data into a joint inversion for 2-D or 3-D P-wave velocity structure and Moho depth using the tomographic modeling algorithm `simulr16` (Bleibinhaus, 2003; Bleibinhaus and Gebrande, 2006), a task planned for our effort in 2018. Unfortunately, as we reported in our previous final report, that task was not accomplished. We attempted to complete the PmP incorporation task this year. We achieved the following this year in the process of overcoming some of the obstacles to this task, but the available time did not allow completion.

(1) We took a series of steps to make the `simulr16` code functional, starting with unsuccessful compilation attempts on the Mac OS platform (the computer platform available to this project) with `gfortran`, followed by the purchases of both Absoft FORTRAN and Intel FORTRAN. All three failed with segmentation faults that could be identified in terms of the responsible code line but could not be resolved.

(2) Discretionary funds of the PI were used to acquire a high-performance Dell laptop on which the CentOS LINUX operating system was installed, and on which the `simulr16` code was successfully compiled and executed on an example dataset.

(3) We turned our attention to acquiring USGS active-source data from Alaska for use in the inversion. The only dataset including PmP arrivals that could be obtained was for the USGS TACT Brooks Range experiment. Our contacts in the USGS were unable to provide PmP data from any other project in Alaska.

(4) Our next step was to prepare the active-source data from Alaska for use in the inversion. Unfortunately, the travel time data were provided only as spreadsheets of offset distance from a particular shot and (reduced) travel time. For use in a tomographic inversion incorporating both active-source and earthquake data, the identity of the receivers and not just offsets are required in order to be able to use actual geographic coordinates. With substantial effort, codes were written to match shot offset values to receivers and construct tables of travel times including the receiver identities. Doing this accurately required modifying the Range FORTRAN algorithm (J. Luetgert, pers. comm.) to process long lists of coordinate pairs (shots and receivers).

Ultimately, all the Brooks Range PmP data were processed successfully, but the time required to accomplish all this left no time for the challenge of carrying out the joint inversion of the active-source and earthquake data, which in turn prevented us from taking the next step of incorporating receiver function data.

Task (f): Release of Alaska CVM version 1.0.

The two models based on the two inversion codes are in the process of being submitted to the IRIS Earth Model Collaboration where they can be freely accessed. IRIS requires information on this report number and DOI as part of the submission, otherwise the necessary files are ready. Availability of the models will be announced via email to known interested parties - USGS scientists with interests in Alaska and other scientists who have recently produced their own models of Alaska seismic velocity structure. Funds are not available to publish our results in a professional journal, so we will also set up access to the models on a University of Wisconsin-Madison web page and/or on Zenodo.

## References

- Abers, G. A., A. N. Adams, P. J. Haeussler, E. Roland, P. J. Shore, D. A. Wiens, S. Y. Schwartz, A. F. Sheehan, D. J. Shillington, S. Webb, and L. L. Worthington (2019), Examining Alaska's earthquakes on land and sea, *Eos*, 100, <https://doi.org/10.1029/2019EO117621>.
- Bensen, G. D., M. H. Ritzwoller, M. P. Barmin, A. L. Levshin, F. Lin, M. P. Moschetti, N. M. Shapiro, and Y. Yang (2007), Processing seismic ambient noise data to obtain reliable broadband surface wave dispersion measurements, *Geophys. J. Int.*, 169, 1,239-1,260. doi: 10.1111/j.1365-246X.2007.03374.x.
- Berg, E. M., F.-C. Lin, A. Allam, V. Schulte-Pelkum, K. M. Ward, and W. Shen (2020), Shear velocity model of Alaska via joint inversion of Rayleigh wave ellipticity, phase velocities, and receiver functions across the Alaska Transportable Array, *J. Geophys. Res.: Solid Earth*, 125, e2019JB018582, <https://doi.org/10.1029/2019JB018582>.
- Bleibinhaus, F. (2003), Entwicklung einer simultanen refraktions- und reflexionsseismischen 3D-Laufzeittomographie mit Anwendung auf tiefenseismische TRANSALP-Weitwinkeldaten aus den Ostalpen, Ph.D. thesis, Univ. Munich, 171 pp.
- Bleibinhaus, F., and H. Gebrande (2006), Crustal structure of the Eastern Alps along the TRANSALP profile from wide-angle seismic tomography, *Tectonophys.*, 414, 51-69. <https://doi.org/10.1016/j.tecto.2005.10.028>.
- Brocher, T. M. (2005), Empirical relations between elastic wavespeeds and density in the Earth's crust, *Bull. Seism. Soc. Am.*, 95, 2081-2092, doi: 10.1785/0120050077.
- Eberhart-Phillips, D. (1989), Investigations of crustal structures and active tectonic processes in the Coast Ranges, Central California, *Geophysics. Stanford Univ.*, Stanford, CA, 209 pp.
- Eberhart-Phillips, D. (1990), Three-dimensional P and S velocity structure in the Coalinga region, California, *J. Geophys. Res.*, 95, 15,343-15,363.
- Eberhart-Phillips, D., S. Bannister, and S. Ellis (2014), Imaging P and S attenuation in the termination region of the Hikurangi subduction zone, New Zealand, *Geophys. J. Int.*, 198, 516-536.
- Eberhart-Phillips, D., D. H. Christensen, T. M. Brocher, R. Hansen, N. A. Ruppert, P. J. Haeussler, and G. A. Abers (2006), Imaging the transition from Aleutian subduction to Yakutat collision in central Alaska, with local earthquakes and active source data, *J. Geophys. Res.*, 111, B11303, doi:10.1029/2005JB004240.
- Eberhart-Phillips, D., and W. Fry (2017), A new scheme for joint surface wave and earthquake travel-time inversion and resulting 3-D velocity model for the western North Island, New Zealand, *Phys. Earth Planet. Inter.*, 269, 98-111, <https://doi.org/10.1016/j.pepi.2017.05.014>.
- Eberhart-Phillips, D., A. Nayak, N. Ruppert, and C. Thurber (2019), Alaska 2018 update for USGS18AP00017: Initial Development of Alaska Community Seismic Velocity Models [Data set], Zenodo, [doi.org/10.5281/zenodo.2544925](https://doi.org/10.5281/zenodo.2544925).
- Eberhart-Phillips, D., and M. Reyners (1997), Continental subduction and three-dimensional crustal structure: The northern South Island, New Zealand, *J. Geophys. Res.*, 102, 11,843-11,861.
- Eberhart-Phillips, D., and M. Reyners (2012), Imaging the Hikurangi plate interface region with improved local-earthquake tomography. *Geophys. J. Int.*, 190, 1221-1242, DOI: 10.1111/j.1365-246X.2012.05553.x.
- Eberhart-Phillips, D., M. Reyners, S. Bannister, M. Chadwick, and S. Ellis (2010), Establishing a versatile 3-D seismic velocity model for New Zealand, *Seism. Res. Lett.* 81, 992-1000, DOI: 10.1785/gssrl.81.6.992.

- Fang, H., H. Yao, H. Zhang, Y.-C. Huang, and R. D. van der Hilst (2015), Direct inversion of surface wave dispersion for three-dimensional shallow crustal structure based on ray tracing: methodology and application, *Geophys. J. Int.*, 201, 1251-1263, DOI: <https://doi.org/10.1093/gji/ggv080>.
- Fang, H., H. Zhang, H. Yao, A. Allam, D. Zigone, Y. Ben-Zion, C. Thurber, and R. D. van der Hilst (2016), A new algorithm for three-dimensional joint inversion of body wave and surface wave data and its application to the Southern California plate boundary region, *J. Geophys. Res. Solid Earth*, 121, 3557-3569, doi:10.1002/2015JB012702.
- Herrmann, R. B. (2013), Computer programs in seismology: An evolving tool for instruction and research, *Seism. Res. Lett.*, 84, 1081-1088, doi: <https://doi.org/10.1785/0220110096>.
- Lanza, F., C. J. Chamberlain, K. Jacobs, E. Warren-Smith, H. J. Godfrey, M. Kortink, C. H. Thurber, M. Savage, J. Townend, S. Roecker, and D. Eberhart-Phillips (2019), Crustal fault connectivity of the Mw 7.8 2016 Kaikōura earthquake constrained by aftershock relocations, *Geophys. Res. Lett.*, 46, 6487-6496. <https://doi.org/10.1029/2019GL082780>.
- Lee, E.-J., P. Chen, T. H. Jordan, P. J. Maechling, M. A. M. Denolle, and G. C. Beroza (2014), Full 3-D tomography for crustal structure in Southern California based on the scattering-integral and the adjoint-wavefield methods, *J. Geophys. Res. Solid Earth*, 119, doi:10.1002/2014JB011346.
- Li, J., G. A. Abers, Y. H. Kim, and D. Christensen (2013), Alaska megathrust 1: Seismicity 43 years after the great 1964 Alaska megathrust earthquake, *J. Geophys. Res.*, 118, 4861-4871, doi:10.1002/jgrb.50358.
- Lin, F.-C., V. C. Tsai, and B. Schmandt (2014), 3-D crustal structure of the western United States: application of Rayleigh-wave ellipticity extracted from noise cross-correlations, *Geophys. J. Int.*, 198, 656-670, <https://doi.org/10.1093/gji/ggu160.s>
- Lin, F.-C., M. P. Moschetti, and M. H. Ritzwoller (2008), Surface wave tomography of the western United States from ambient seismic noise: Rayleigh and Love wave phase velocity maps, *Geophys. J. Int.*, doi:10.1111/j.1365-246X.2008.03720.x.
- Maceira, M., and C. J. Ammon (2009), Joint inversion of surface wave velocity and gravity observations and its application to central Asian basins shear velocity structure, *J. Geophys. Res.*, 114, B02314, <http://dx.doi.org/10.1029/2007JB005157>.
- Pavlis, N. K., S. A. Holmes, S. C. Kenyon, and J. K. Factor (2012), The development and evaluation of the Earth Gravitational Model 2008 (EGM 2008), *J. Geophys. Res.* 117, B04406, <http://dx.doi.org/10.1029/2011JB008916>.
- Rawlinson, N., and M. Sambridge (2004), Wave front evolution in strongly heterogeneous layered media using the fast marching method, *Geophys. J. Int.*, 156, 631-647, <https://doi.org/10.1111/j.1365-246X.2004.02153.x>.
- Ruppert, N., A. Nayak, C. Thurber, and C. Richards (2020), Aftershock analysis of the 2018 Mw 7.1 Anchorage, Alaska, earthquake: Relocations and regional moment tensors, *Seism. Res. Lett.*, 91, 114-125.
- Shellenbaum, D. P., L. S. Gregersen, and P. R. Delaney (2010), Top Mesozoic unconformity depth map of the Cook Inlet Basin, Alaska, Alaska Div. Geol. Geophys. Surv. Report of Investigation 2010-2, 1 sheet, Scale 1:500,000.
- Shaw, J. H., A. Plesch, C. Tape, M. P. Suess, T. H. Jordan, G. Ely, E. Hauksson, J. Tromp, T. Tanimoto, R. Graves, K. Olsen, C. Nicholson, P. J. Maechling, C. Rivero, P. Lovely, C. M. Brankman, and J. Munster (2015), Unified Structural Representation of the southern



- California crust and upper mantle, *Earth Planet. Sci. Lett.* 415, doi: 10.1016/j.epsl.2015.01.016.
- Steck, L. K., and W. A. Prothero Jr. (1991), A 3-D raytracer for teleseismic body-wave arrival times, *Bull. Seism. Soc. Am.*, 81, 1332-1339.
- Syracuse, E. M., H. Zhang, and M. Maceira (2017), Joint inversion of seismic and gravity data for imaging seismic velocity structure of the crust and upper mantle beneath Utah, United States, *Tectonophysics*, 718, 105-117, <http://dx.doi.org/10.1016/j.tecto.2017.07.005>.
- Tape, C., D. Christensen, M. M. Moore-Driskell, J. Sweet, and K. Smith (2017), Southern Alaska Lithosphere and Mantle Observation Network (SALMON): A seismic experiment covering the active arc by road, boat, plane, and helicopter, *Seism. Res. Lett.*, 88, 1185-1202, doi:10.1785/0220160229.
- Thurber, C. H. (1983), Earthquake locations and three-dimensional crustal structure in the Coyote Lake area, central California, *J. Geophys. Res.: Solid Earth*, 88, 8226-8236.
- Thurber, C., and D. Eberhart-Phillips (1999), Local earthquake tomography with flexible gridding, *Comp. & Geosci.*, 25, 809-818.
- Zhang, H., and C. H. Thurber (2003), Double-difference tomography: the method and its application to the Hayward fault, California, *Bull. Seism. Soc. Am.*, 93, 1875-1889.
- Zhang, H., C. Thurber, D. Shelly, S. Ide, G. Beroza, and A. Hasegawa (2004), High-resolution subducting slab structure beneath Northern Honshu, Japan, revealed by double-difference tomography, *Geology*, 32, 361-364.

#### **(4) Project Data**

We will announce the availability of our two Alaska Community Velocity Models, which will be accessible through the IRIS Earth Model Collaboration (EMC). We have begun the process of creating EMC-compatible model files. Any data used will be provided to anyone requesting it. We will also consider creating a Zenodo web page with the data, if that is possible for the very large dataset involved.

#### **(5) Bibliography**

Ruppert, N., A. Nayak, C. Thurber, and C. Richards (2020), Aftershock analysis of the 2018 Mw 7.1 Anchorage, Alaska, earthquake: Relocations and regional moment tensors, *Seism. Res. Lett.*, 91, 114-125.

#### **(6) Acknowledgement of Support and Disclaimer**

This material is based upon work supported by the U.S. Geological Survey under Grant No. G19AP00019.

The views and conclusions contained in this document are those of the authors and should not be interpreted as representing the opinions or policies of the U.S. Geological Survey. Mention of trade names or commercial products does not constitute their endorsement by the U.S. Geological Survey.